Materials Today Advances 30 (2026) 100810

Contents lists available at ScienceDirect

Materials Today Advances

journal homepage: www.journals.elsevier.com/materials-today-advances/

Nanostructured SERS-AI integration for noninvasive biochemical detection and disease classification in retinal vascular and chorioretinal diseases

Sanghwa Lee [a,1], Yong-Ha Jo [b,1], Kyeong Ryeol Kim [c], Junyeop Lee [b,d,*], Jun Ki Kim [a,c,e,f,**]

[a] Biomedical Engineering Research Center, Asan Medical Center, Seoul, 05505, Republic of Korea
[b] Department of Ophthalmology, Asan Medical Center, College of Medicine, University of Ulsan, Seoul, 05505, Republic of Korea
[c] Department of Convergence Medicine, University of Ulsan, College of Medicine, Seoul, 05505, Republic of Korea
[d] Graduate School of Health Science and Technology, UNIST, Ulsan, 44919, Republic of Korea
[e] Institute of Digital Healthcare, University of Ulsan College of Medicine, Seoul, 05505, Republic of Korea
[f] Apollon, Inc., Seoul, 07797, Republic of Korea

ARTICLE INFO

Keywords:
Retinal vascular disease
Aqueous humor
Surface-enhanced Raman spectroscopy
Machine learning
Anti-VEGF response
Principal component analysis
Nano Biomarker-based diagnosis

ABSTRACT

Retinal and choroidal vascular diseases, such as retinal vein occlusion, diabetic macular edema, central serous chorioretinopathy, and wet age-related macular degeneration, are major causes of irreversible vision loss across diverse age groups. Conventional imaging provides structural but not molecular information, often delaying the opportunity to modify ineffective regimens. We developed an integrated diagnostic platform combining surface-enhanced Raman spectroscopy (SERS) with machine learning algorithms for label-free biochemical profiling of retinal diseases. Reproducible AI-interpretable spectral features were extracted from microliter-scale aqueous humor (AH) samples using gold-coated ZnO nanorod SERS chips. The nanostructured substrate acted as an electromagnetic field enhancer, amplifying Raman signals to enable data-driven disease classification directly from trace biofluids.

We implemented a multi-stage AI framework incorporating support vector machine (SVM), linear (LDA), and quadratic discriminant analysis (QDA) to optimize clinical workflows. The PC-SVM model achieved an outstanding primary screening accuracy of 96.45%, with a 10-fold cross-validation (CV) accuracy of 92.93% and an area under the curve (AUC) of 0.994. PC-LDA and PC-QDA models reached stable 10-fold CV scores of 87.63% and 86.45%, respectively, demonstrating high resistance to overfitting and strong generalizability across disease phenotypes. Responder prediction for anti-VEGF therapy exceeded 90% accuracy before visible anatomical improvement, confirming that biochemical alterations precede structural recovery.

This AI-assisted SERS platform provides a rapid, minimally invasive strategy for biochemical profiling and therapeutic monitoring of retinal diseases. This technology bridges the gap between structural biomarkers and true biochemical disease activity, offering a point-of-care tool for personalized ophthalmic care and real-time treatment guidance in clinical settings.

1. Introduction

Retinal and choroidal vascular diseases, including retinal vein occlusion (RVO), diabetic macular edema (DME), central serous chorioretinopathy (CSC), and wet age-related macular degeneration (wAMD), represent a major global ophthalmic health burden across diverse age groups. These conditions frequently result in progressive and irreversible vision loss if not diagnosed and managed promptly. RVO and DME are characterized by vascular leakage and intraretinal fluid accumulation, whereas CSC and wAMD involve subretinal fluid or neovascularization, resulting in visual distortion and retinal damage. Epidemiological studies indicate that these diseases affect millions worldwide and are associated with decreased quality of life and substantial healthcare utilization [1] (see Scheme 1).

* Corresponding author. Department of Ophthalmology, Asan Medical Center, College of Medicine, University of Ulsan, Seoul, 05505, Republic of Korea.
** Corresponding author. Biomedical Engineering Center, ASAN Institute for Life Sciences, Asan Medical Center, Songpa-gu, Seoul, 05505, Republic of Korea.
E-mail addresses: j.lee@amc.seoul.kr (J. Lee), kim@amc.seoul.kr (J.K. Kim).
[1] Sanghwa Lee and Yong-Ha Jo contributed equally to this study as first authors.

https://doi.org/10.1016/j.mtadv.2026.100810
Received 22 January 2026; Received in revised form 21 April 2026; Accepted 5 May 2026
Available online 20 May 2026

In clinical practice, significant proportion of patients visiting ophthalmic clinics present with vision loss, primarily attributed to age-related cataracts [2]. However, coexisting retinal vascular pathologies often complicate surgical prognosis and limit postoperative visual recovery [3]. For instance, performing cataract surgery without prior detection of macular edema or neovascularization can exacerbate inflammatory responses, potentially leading to irreversible structural damage and suboptimal functional gains [4]. Therefore, rapid screening and biochemical validation are crucial for differentiating these high-risk retinal conditions from routine cataracts, ensuring that patients receive appropriate pretreatment or concurrent management to optimize long-term visual outcomes [5]. Timely diagnosis and tailored therapy, such as intravitreal anti-VEGF injection, are essential to prevent irreversible photoreceptor damage [6].

Despite the widespread clinical use of optical coherence tomography (OCT), fluorescein angiography, and fundus photography, these imaging techniques primarily provide structural and anatomical information and remain insufficient for capturing the biochemical dynamics underlying disease progression or therapeutic response. In current clinical practice, 30–40% of patients exhibit suboptimal or delayed responses to anti-VEGF therapy [7,8], a phenomenon often attributed to unrecognized biochemical heterogeneity within retinal microenvironments. Moreover, treatment responsiveness is typically assessed one month after injection, delaying the opportunity to modify ineffective regimens [9,10]. This limitation underscores the urgent need for an analytical approach to detect early biochemical alterations preceding visible anatomical changes.

Integrating surface-enhanced Raman spectroscopy (SERS) with AI-driven spectral interpretation can address these challenges by bridging the gap between molecular pathology and imaging-based diagnostics. SERS enables ultrasensitive detection of biochemical alterations through photon–molecule interactions, capturing vibrational spectra that reflect subtle metabolic or inflammatory changes. When enhanced by metallic nanostructures such as gold-coated ZnO nanorods, the local electromagnetic field (localized surface plasmon resonance, LSPR) amplifies Raman scattering, enabling high-fidelity spectral acquisition from minute fluid volumes by several orders of magnitude. This technology has been applied in previous studies for disease diagnosis in biological systems. Blood-based SERS profiling sensitively monitored systemic metabolic alterations associated with atherosclerosis and multi-organ injury [11–13]. Urine-derived spectral biomarkers have been utilized for the early diagnosis of renal injury and bladder cancer [14]. Our research group further validated the clinical robustness of SERS-AI analysis for noninvasive monitoring of kidney transplant rejection, achieving high diagnostic accuracy from minimal patient samples [15]. These findings collectively substantiate the clinical validity and reliability of SERS as a molecular-level diagnostic and monitoring platform, providing a solid foundation for its application to ocular biofluids where sample availability is extremely limited.

Unlike blood or urine, ocular biofluids including aqueous and vitreous humor exist in a viscous, gel-like matrix that tightly entraps biomolecules. Extracting these molecules without chemical dilution or

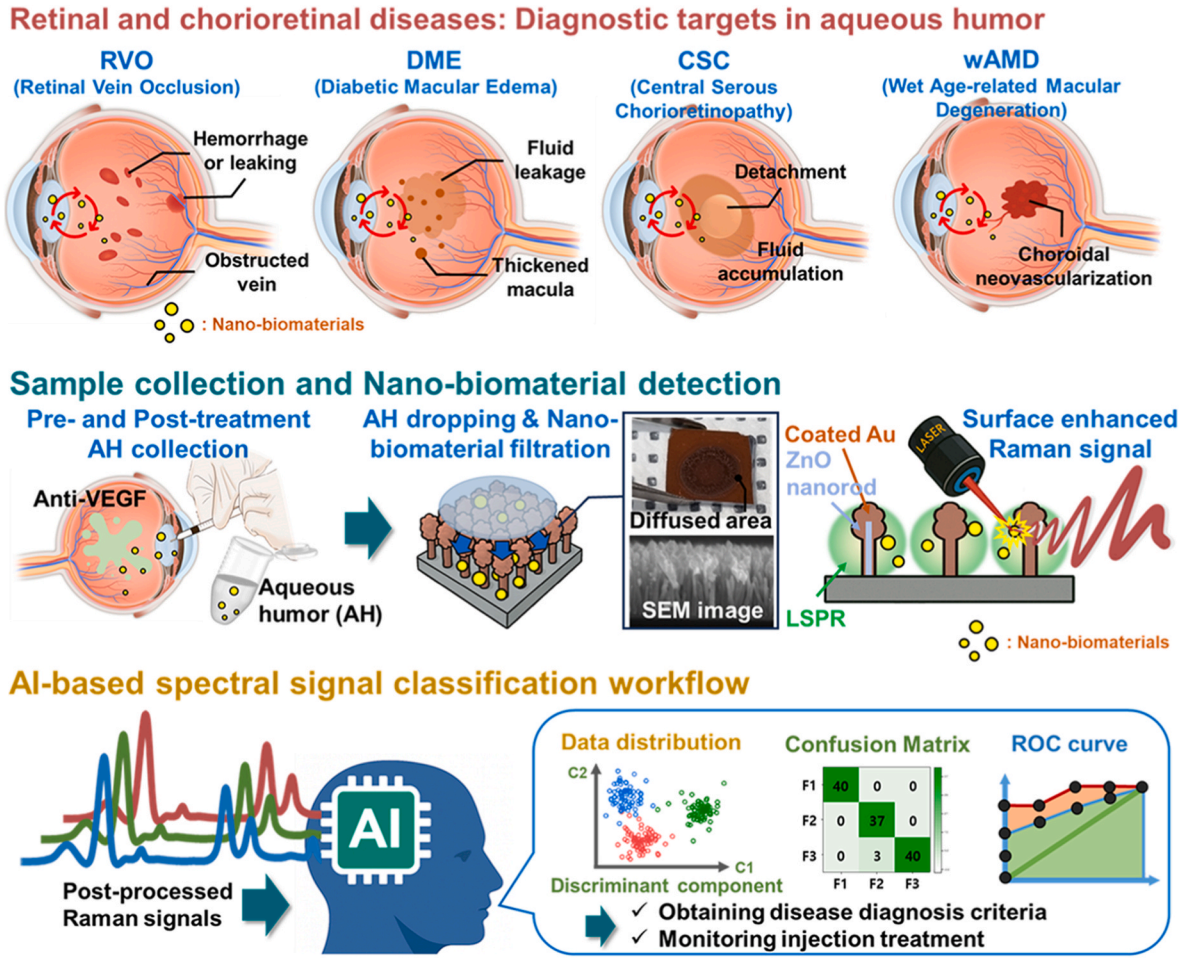

Scheme 1. Schematic representation of a diagnostic workflow that classifies retinal vein occlusion (RVO), diabetic macular edema (DME), central serous chorioretinopathy (CSC), and wet age-related macular degeneration (wAMD) using Raman spectra from aqueous humor samples
Gold-coated ZnO nanorod substrates are used to enhance molecular signals through surface-enhanced Raman scattering. Spectral data are processed with machine learning algorithms to extract disease-specific features and evaluate treatment response.

enzymatic digestion risks contamination or loss of diagnostic information [16,17]. Traditional biochemical assessments, particularly mass spectrometry-based proteomics, typically require a substantial volume of aqueous humor (~100 μL) for reliable analysis [18,19]. However, even with this volume, samples often undergo extensive chemical dilution and complex pre-processing, increasing the risk of losing trace biomarkers and compromising diagnostic integrity [18,19]. Furthermore, the entire procedure involves intricate multi-step preparation and data acquisition and can span several days to weeks, limiting its utility for rapid clinical decision-making [20]. Most importantly, extracting ~100 μL of fluid poses a significant clinical burden as it can drastically alter intraocular pressure (IOP), potentially resulting in adverse ocular effects [21]. Consequently, a sensing platform capable of direct, high-sensitivity analysis from microliter-scale fluid samples is indispensable. Our platform enables real-time acquisition of enhanced spectral signals by utilizing only a few microliters of raw sample without any dilution or pre-treatment, offering dramatic clinical utility. The gold-coated ZnO nanorod substrate fulfills this role by acting as a nanoscale biofilter and signal amplifier simultaneously, enabling selective enrichment of nano-biomarkers and reproducible spectral acquisition even from trace biofluid volumes.

In this study, we present an integrated nanoplasmonic and AI-assisted diagnostic framework for label-free, minimally invasive, and high-sensitivity biochemical profiling of retinal and choroidal vascular diseases. SERS enhanced via gold-coated ZnO nanorod substrates was employed to analyze microliter-scale aqueous humor samples collected from patients diagnosed with RVO, DME, CSC, or wAMD and age-matched healthy controls. These nanostructured SERS substrates function as electromagnetic amplifiers and molecular sieves, enabling the enrichment and detection of nano-biomarkers entrapped within the viscous ocular biofluid matrix without chemical preprocessing.

The resulting vibrational spectra, rich in disease-relevant biochemical signatures, were processed using AI-based classification algorithms including principal component analysis (PCA), linear discriminant analysis (LDA), and quadratic discriminant analysis (QDA). This computational pipeline enabled precise differentiation of disease states and prediction of therapeutic response patterns, even prior to the emergence of anatomical changes detected by OCT or angiography. While SERS-based diagnostics have demonstrated strong translational value in oncology, microbiology, and metabolic disease, their adaptation to ophthalmology via this nanoplasmonic-AI platform introduces novel avenues for early diagnosis, personalized treatment planning, and real-time therapeutic monitoring in retinal diseases.

2. Methods

2.1. Study population and clinical evaluation

In this prospective study, treatment-naïve patients aged >18 years who were scheduled for intravitreal injections due to retinal and choroidal vascular diseases were recruited from the Department of Ophthalmology, Asan Medical Center, between January 2025 and May 2025. Aqueous humor (AH) samples were collected from patients diagnosed with retinal vascular diseases, including RVO, DME, CSC, and wAMD. The control group was expanded and refined to include patients undergoing cataract surgery without any retinal disease. The control group was strategically composed of both non-diabetic individuals and patients with diabetes without clinical evidence of diabetic retinopathy to ensure that the identified biochemical signatures were disease-specific rather than attributable to systemic metabolic backgrounds. This enabled a more rigorous differentiation between high-risk retinal conditions and routine cataract cases, particularly in patients with pre-existing systemic comorbidities such as diabetes. The study was conducted in accordance with the principles outlined in the Declaration of Helsinki. Ethical approval was granted by the Institutional Review Board (IRB) of Asan Medical Center (IRB approval number: 2025-0575). Written informed consent was obtained from all participants or their legal guardians prior to enrollment.

All participants (N = 38) underwent comprehensive ophthalmic evaluation prior to aqueous humor sampling, following a standardized multimodal imaging protocol including best-corrected visual acuity (BCVA), tonometry, color fundus photography, spectral-domain optical coherence tomography (SD-OCT; Spectralis HRA + OCT, Heidelberg Engineering, Germany), fluorescein angiography (FA), and fundus autofluorescence (FAF). Patients were classified into the four disease groups based on these imaging findings, along with a control group. The specific group sizes were RVO (n = 5), DME (n = 10), CSC (n = 5), and wAMD (n = 6). The classification was independently validated by two retina specialists, and discrepancies were resolved by consensus. Patients with ambiguous or uncertain diagnoses or those for whom two independent retina specialists did not agree on the assessment were excluded from the study. Additional exclusion criteria included a history of prior intravitreal injections, significant retinal pathologies other than the target diseases, high myopia, or advanced glaucoma.

Baseline demographics and systemic comorbidities of the study population are summarized in Table 1. Age, sex, hypertension, hyperlipidemia, diabetes status, and HbA1c levels were recorded from electronic medical records at the time of enrollment. No significant intergroup differences were observed in age or sex distribution ($p > 0.05$), whereas disease-specific systemic backgrounds, such as the presence of diabetes in patients with DME, were consistent with known epidemiologic trends.

Anatomical and functional parameters were followed at 1-month and 6-month post-injection visits to assess pharmacological efficacy. OCT-derived parameters, including pre-injection central subfield thickness (CST) and BCVA (logMAR), were measured immediately before anti-VEGF administration for diagnostic confirmation and as reference points for therapeutic monitoring. Patients with both CST reduction ≥20% and logMAR improvement ≥0.1 in BCVA were classified as responders, whereas those with minimal or no improvement were designated as non-responders. Serial CST and BCVA trends, illustrated in Fig. 1, exhibit distinct recovery patterns across disease subtypes and response categories, providing objective clinical validation for comparison with Raman spectral biomarkers.

2.2. Fabrication of gold-coated ZnO nanorod arrays for ophthalmic SERS applications

To construct a high-sensitivity SERS substrate optimized for ocular biofluid analysis, vertically oriented ZnO nanorods were synthesized and subsequently coated with a uniform gold layer to amplify Raman scattering via localized plasmonic resonance. Initially, a ZnO nucleation layer (approximately 30 nm thick) was deposited onto a pre-cleaned silicon wafer. Subsequently, controlled hydrothermal growth was employed to generate aligned ZnO nanostructures with an average rod length of 300–400 nm and a diameter of approximately 30 nm.

Growth was conducted in an aqueous precursor solution containing 50 mM zinc nitrate hexahydrate and 50 mM ammonium hydroxide (Sigma Aldrich, St. Louis, MO, USA), dissolved in 25 mL of deionized water. The seeded wafers were incubated at 90 °C for 90 min. Following nanorod formation, thermal evaporation (Alpha Plus Co., Seoul, Korea) was used to deposit a 200 nm-thick gold layer, monitored in real time using a quartz crystal microbalance.

The completed Au–ZnO nanorod arrays were characterized by field emission scanning electron microscopy (FE-SEM, JSM-7001F, JEOL, Japan) at 10 kV to confirm vertical alignment and sub-100 nm nanogap morphology. Previous studies have indicated that nanogap uniformity and metallic coating thickness are key determinants of SERS performance; these considerations informed the fabrication parameters employed in this protocol.

Transmission electron microscopy (TEM) analysis was performed using a JEM-2100F system (JEOL, Japan) operated at 200 kV to further

Table 1
Baseline characteristics of responders and non-responders in each disease group.

	DME		RVO		wAMD		CSC	
	Responder (n = 5)	Non-responder (n = 5)	Responder (n = 3)	Non-responder (n = 2)	Responder (n = 3)	Non-responder (n = 3)	Responder (n = 2)	Non-responder (n = 3)
Age (median, range)	55 (52–75)	65 (57–67)	79 (79–81)	68 (62–76)	84 (79–84)	69 (67–73)	54.5 (33–76)	43 (43–56)
Age (mean ± SD)	61.4 ± 10.8	64.0 ± 4.1 (p = 0.63)	79.7 ± 1.2	68.7 ± 7.0 (p = 0.11)	82.3 ± 2.9	69.1 ± 3.1 (p = 0.005)	54.5 ± 30.4	47.3 ± 7.5 (p = 0.33)
Sex								
Female	3 (60.0 %)	4 (80.0 %)	2 (66.7 %)	2 (66.7 %)	2 (66.7 %)	1 (33.3 %)	0 (0.0 %)	1 (33.3 %)
Male	2 (40.0 %)	1 (20.0 %)	1 (33.3 %)	1 (33.3 %)	1 (33.3 %)	2 (66.7 %)	2 (100.0 %)	2 (66.7 %)
Hypertension								
Y	2 (40.0 %)	4 (80.0 %)	2 (66.7 %)	2 (66.7 %)	2 (66.7 %)	0 (0.0 %)	0 (0.0 %)	0 (0.0 %)
N	3 (60.0 %)	1 (20.0 %)	1 (33.3 %)	1 (33.3 %)	1 (33.3 %)	3 (100.0 %)	3 (100.0 %)	3 (100.0 %)
Hyperlipidemia								
Y	0 (0.0 %)	2 (40.0 %)	2 (66.7 %)	2 (66.7 %)	1 (33.3 %)	0 (0.0 %)	0 (0.0 %)	0 (0.0 %)
N	5 (100.0 %)	3 (60.0 %)	1 (33.3 %)	1 (33.3 %)	2 (66.7 %)	3 (100.0 %)	3 (100.0 %)	3 (100.0 %)
Diabetes								
Y	5 (100.0 %)	5 (100.0 %)	0 (0.0 %)	0 (0.0 %)	0 (0.0 %)	0 (0.0 %)	0 (0.0 %)	0 (0.0 %)
N	0 (0.0 %)	0 (0.0 %)	3 (100.0 %)	3 (100.0 %)	3 (100.0 %)	3 (100.0 %)	3 (100.0 %)	3 (100.0 %)
HbA1c (%)	8.28 ± 2.23	6.38 ± 0.69 (p = 0.13)						
Pre-injection BCVA (logMAR)	0.59 ± 0.40	0.47 ± 0.49 (p = 0.68)	0.74 ± 1.15	2.10 ± 0.17 (p = 0.17)	0.48 ± 0.24	0.42 ± 0.17 (p = 0.72)	0.05 ± 0.07	0.23 ± 0.40 (p = 0.57)
Pre-injection IOP (mmHg)	16.0 ± 4.21	14.8 ± 2.93 (p = 0.63)	13.3 ± 1.53	13.3 ± 1.15 (p = 1.00)	14.0 ± 3.61	14.7 ± 2.08 (p = 0.79)	12.5 ± 3.54	12.3 ± 3.51 (p = 0.95)
Pre-injection CST (μm)	543.4 ± 98.5	541.4 ± 95.4 (p = 0.97)	435.0 ± 195.6	842.7 ± 383.2 (p = 0.19)	305.7 ± 129.0	483.0 ± 76.7 (p = 0.09)	400.5 ± 26.2	489.3 ± 112.6 (p = 0.41)

RVO: retinal vein occlusion; DME: diabetic macular edema; CSC: central serous chorioretinopathy; wAMD: wet age-related macular degeneration; BCVA: best-corrected visual acuity; IOP: intraocular pressure; CST: central subfield thickness.

validate the porous architecture and nanoscale Au distribution within the SERS platform. Site-specific cross-sectional specimens were prepared via focused ion beam milling (Nova Nanolab, FEI, USA), enabling precise extraction and thinning of individual nanorod domains to levels of electron transparency. Processed sections were transferred onto carbon-coated copper grids and dried under ambient conditions prior to imaging. TEM examination confirmed the vertically aligned porous morphology of ZnO cores and conformal Au coating along the nanorod surfaces. Energy-dispersive X-ray spectroscopy (EDS) mapping was subsequently conducted to assess elemental distribution within the arrays, enabling visualization of the spatial localization of Au, Zn, and O throughout the nanorod structures.

2.3. SERS acquisition from aqueous humor samples in patients with retinal disease

AH samples (volume: 100 μL) were collected from patients diagnosed with RVO, DME, CSC, or wAMD at scheduled clinical time points, either prior to intravitreal injection or during anterior chamber paracentesis under sterile surgical conditions. All samples were immediately transferred to sterile microcentrifuge tubes and stored at −80 °C until Raman analysis. No preservative agents were added to prevent interference with Raman signal acquisition.

For each patient, a 5 μL aliquot of the AH sample was pipetted onto the surface of the prepared SERS substrate. All specimens were analyzed within 30 min of sample application to preserve molecular integrity. One SERS chip was used per patient per time point, and 20 spectra were acquired from separate regions of the dried sample to capture intra-sample variability.

Spectral acquisition was performed using an upright Raman microspectroscopy system (FEX-INV, WEVE, Seoul, South Korea) equipped with a 785 nm excitation diode laser (laser output: 10 mW). Raman signals were collected through a 40 × objective lens and dispersed by a 600 grooves/mm grating. Each spectrum was captured with a 4-s exposure, and the signal was averaged over 10 frames to improve signal-to-noise characteristics.

Prior to analysis, the spectrometer was calibrated using a silicon crystal as an internal standard. Background correction and denoising were performed using an in-house software (RAON-Vu, WEVE, Korea). A polynomial fitting approach (fifth-order) was used to subtract baseline fluorescence, followed by application of the Savitzky–Golay filter for spectral smoothing. Final spectral datasets were visualized as averaged profiles with shaded standard deviation intervals across disease groups.

2.4. AI-based multiclass analysis of retinal disease spectral signatures

To distill high-dimensional Raman data into diagnostically relevant variables, PCA was implemented across the full dataset, comprising approximately 1004 data points per spectrum at 2 cm^{-1} intervals. Up to 150 principal components (PCs) were retained for further modeling based on their cumulative explained variance.

A total of 520 spectra from the disease cohort and 240 spectra from the control group, totaling 760 independent spectra from 38 participants, were used in classification. Subgroup-specific averages and error margins were computed to assess biochemical heterogeneity across RVO, DME, CSC, and wAMD. PCA score plots were employed to evaluate clustering trends and potential overlaps among disease phenotypes. PCA-derived variables were input into linear and quadratic discriminant analysis (LDA, QDA) and support vector machine (SVM) models for diagnostic classification. These supervised learning models were trained to distinguish between disease classes and controls using stratified spectral datasets.

2.5. Statistical analysis and model validation

Baseline demographics and clinical characteristics, including age, BCVA, and CST, were recorded and compared across groups. Continuous variables were analyzed to determine significant intergroup differences, with p-values >0.05 indicating no significant distribution bias in age or sex.

Model validation included the generation of confusion matrices and receiver operating characteristic (ROC) curves, along with calculating

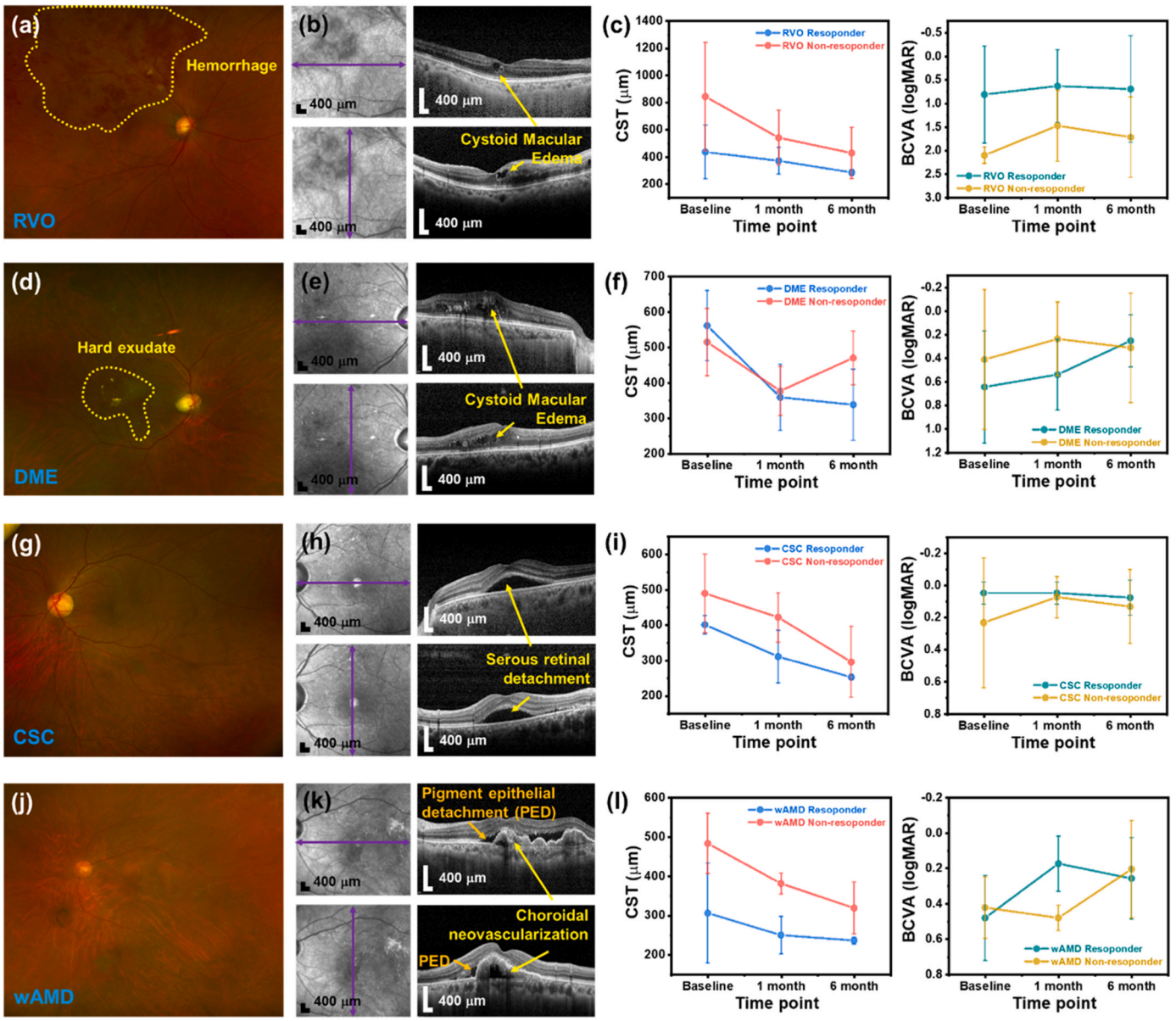

Fig. 1. Representative fundus and optical coherence tomography (OCT) findings with longitudinal treatment responses in retinal vascular diseases
Retinal vein occlusion (RVO): (a) Fundus photograph showing extensive hemorrhage (yellow dotted line) and (b) OCT image revealing cystoid macular edema (CME). (c) Line graphs indicate temporal changes in the clinical response (e.g., BCVA, CST) between responder and non-responder groups. Diabetic macular edema (DME): Presence of hard exudates on (d) fundus image and CME on (e) OCT. (f) Corresponding plots demonstrate differential recovery patterns between DME responders and non-responders. Central serous chorioretinopathy (CSC): (g) Fundus image without prominent exudates but (h) OCT showing serous retinal detachment. (i) Graphs display treatment outcomes distinguishing CSC responder profiles. Wet age-related macular degeneration (wAMD): (j) Fundus image, (k) pigment epithelial detachment (PED) and choroidal neovascularization (CNV) observed on OCT. (l) Response curves show disease-specific therapeutic differences between wAMD responders and non-responders.

diagnostic metrics such as sensitivity, specificity, and area under the curve (AUC) to evaluate screening and classification performance. To rigorously ensure the generalizability of the AI framework and prevent overfitting, a 10-fold cross-validation strategy was implemented, where the dataset was partitioned into training and independent validation sets. All statistical computations were conducted using XLSTAT 2025 (Lumivero, Denver, CO, USA), and all graphs were plotted using Origin 2018 software (OriginLab, Northampton, MA, USA).

3. Results & discussion

3.1. Clinical validation and subgroup classification based on imaging diagnosis

All participants (N = 38) underwent a comprehensive multimodal ophthalmic evaluation constituting color fundus photography, FA, FAF, and spectral-domain OCT, prior to aqueous humor sampling. Participants were stratified into five clinically defined groups based on characteristic imaging phenotypes: RVO (n = 5), DME (n = 10), CSC (n = 5), wAMD (n = 6), and controls without retinal pathology (n = 12). An independent review of all imaging data was conducted by two retina specialists. Final classifications were determined through consensus

agreement to ensure diagnostic accuracy.

Fig. 1 shows representative imaging findings for each group. RVO cases demonstrated extensive retinal hemorrhage and macular edema; DME showed intraretinal cystoid spaces; CSC exhibited serous retinal detachment; and wAMD revealed pigment epithelial detachment or choroidal neovascularization, with associated exudation. Control participants undergoing cataract surgery without retinal disease served as reference comparators.

This imaging-based stratification provided the clinical ground truth for subsequent aqueous humor Raman analysis, enabling direct alignment of structural pathology with molecular signatures. A rigorous framework was established through well-defined subgrouping to evaluate whether nanostructure-enhanced Raman profiles and computational classification models could recapitulate, complement, or extend conventional diagnostic categories.

3.2. Demographic and clinical characteristics of the study population

Baseline demographic and clinical features of the study population are summarized in Table 1. No significant differences were observed among the groups regarding age, sex distribution, systemic comorbidities, or HbA1c levels (all $p > 0.05$). This demographic homogeneity minimized potential confounding effects when comparing aqueous humor molecular profiles across disease and control groups.

OCT-derived anatomical parameters further supported the clinical validity of group-specific phenotypes. CST was markedly elevated in DME and RVO at baseline, consistent with macular edema, whereas CSC showed characteristic serous detachment, and wAMD demonstrated increased retinal thickness associated with exudation or pigment epithelial detachment. The longitudinal changes in CST and BCVA at 1-month and 6-month follow-up are summarized in Table S1 and visualized in Fig. 1. As expected, responders exhibited substantial CST reduction and meaningful visual improvement, whereas non-responders showed limited anatomical recovery and minimal functional gains.

These treatment trajectories confirm that responder and non-responder classifications were grounded in objective clinical assessments. This well-validated clinical dataset provides an essential reference for evaluating whether Raman spectral features and machine learning–based analytical models can identify disease signatures and therapeutic response patterns. These markers may align with or potentially surpass conventional imaging biomarkers.

3.3. Structural basis and acquisition workflow for AH-derived SERS signals on the Au–ZnO nanogap platform

SERS was conducted on AH samples collected from patients diagnosed with RVO, DME, CSC, and wAMD and from age-matched controls. Spectra were acquired on an Au–ZnO nanorod SERS substrate designed for high field enhancement. SEM inspection revealed vertically aligned ZnO nanorods coated with a conformal Au layer, forming inter-rod nanoscale gaps predominantly distributed around ~100 nm. These closely spaced metallic domains act as reproducible SERS-active hotspots, which is further supported by TEM and elemental mapping (Supplementary Fig. S1)

The technical reliability and clinical utility of this Au–ZnO nanostructure have been extensively validated in our previous studies of various biological specimens, including blood, urine, and serum from both animal models and human patients. We verified the batch-to-batch reproducibility across multiple 6-inch wafer batches to ensure operator-independent consistency for clinical translation, as shown in Fig. S2. The calculated relative standard deviation (RSD) at major characteristic peaks remained within a stable range of 15–20%, demonstrating high structural uniformity and fabrication robustness. This structural consistency enables the precise identification of disease-specific biochemical fingerprints, providing a reliable diagnostic foundation based on the comparative analysis of clinical and control groups.

For each AH sample, a microliter-scale droplet was placed onto the chip, where it naturally maintained its hemispherical contour due to surface tension. Upon contacting the Au–ZnO nanorod forest, a portion of the nanoscale biomolecular components immediately interacted with the high-surface-area nanogap network and migrated into the inter-rod spaces through capillary-driven diffusion. This process produced two coexisting regions: the main dried droplet body delineated by its preserved boundary and a nanogap-infiltrated peripheral zone where biomolecules were selectively retained (Supplementary Fig. S3a). To ensure the reliability of molecular profiling, Raman signals were collected from 20 points along this boundary to offset sub-millimeter scale variations and provide stable, reproducible spectral datasets (see Supplementary S3 for details). Under a × 40 objective, the peripheral filtered region was easily identified, and the excitation laser was precisely positioned onto this area using the microscope crosshair (Supplementary Fig. S3b)

Biomolecules retained within the nanogap regions interact with localized plasmonic fields generated by the Au-coated ZnO nanorod clusters. Prior finite element method simulations of similar Au–ZnO architectures have demonstrated that metal clustering around nanorod surfaces produces pronounced local surface plasmon resonance effects. This results in significant field intensification near the nanogap domains [22]. As the SERS enhancement profile is maximized along the axis perpendicular to the incident laser direction, biomolecular components situated within these plasmonically active regions yield markedly amplified Raman signals. This behavior is consistent with the enhancement factor of approximately 3×10^5, measured using Rhodamine B on the Au–ZnO nanogap substrate, as reported in Supplementary Fig. S2, thereby verifying the performance of the nanostructured platform.

3.4. Raman spectral feature extraction and unsupervised evaluation of diagnostic separability

Laser excitation was directed onto the nanobiomarker-filtered region, and scattered light was collected through the microscope-coupled spectroscopic module to obtain individual Raman spectra. Each spectrum captured the vibrational fingerprint across 325–2480 cm^{-1}, reflecting the characteristic biochemical profile at a single measurement point. For each patient, twenty spectra were acquired from distinct positions within the filtered nanobiomaterial diffusion zone to account for local heterogeneity, and these spectra together constituted one data unit for analysis. The group-level mean profiles and standard deviations were subsequently computed from all aggregated patient spectra.

Representative spectra for each group are shown in Fig. 2a, with bold lines indicating mean values and shaded regions denoting the standard deviation. Although the overall spectral profiles followed a similar baseline, several distinctive peaks exhibited noticeable intensity trends at multiple diagnostic bands. In particular, while individual samples showed variability within the standard deviation, the mean spectra revealed prominent trending signals at approximately 501, 640, 1135, and 1655 cm^{-1}, corresponding to glycine, tyrosine (aromatic ring vibration), serine (protein C-N/C-C stretching), and fatty acid/Amide I, respectively. Full peak assignments are summarized in Table 2, annotated based on prior Raman biochemical studies of biofluids and established reference databases.

Although the mean spectral profiles exhibited distinct intensity trends at specific diagnostic bands, individual raw spectra collected from different measurement points showed significant overlap within the standard deviation ranges. This inherent biochemical heterogeneity challenges the differentiation of groups based on simple visual inspection of single spectral profiles, despite the differences observed in their averaged representations. Unsupervised dimensionality reduction via PCA was applied to quantitatively evaluate the similarity between these high-dimensional data points and assess the intrinsic clustering behavior of individual spectra. PCA score plots based on the top three components exhibited substantial intergroup overlap, as shown in Fig. 2b. Although

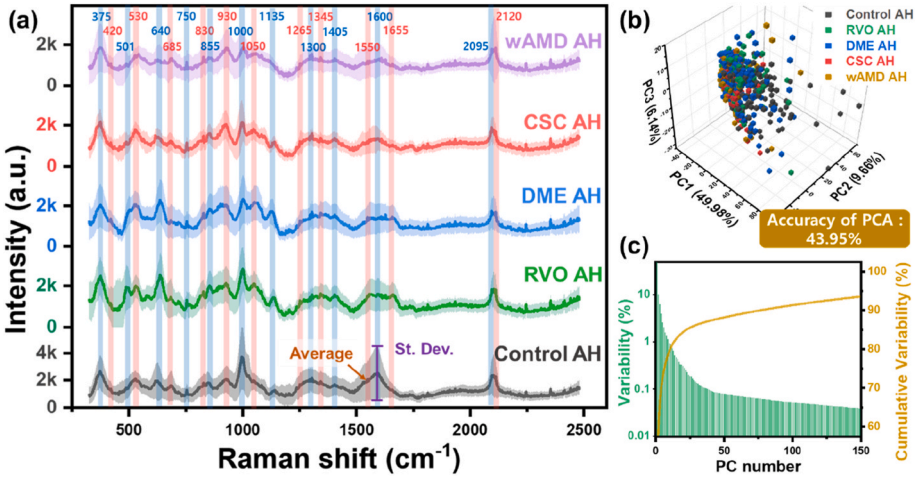

Fig. 2. (a) Surface-enhanced Raman spectra of aqueous humor (AH) samples from control eyes and from patients with retinal vein occlusion (RVO), diabetic macular edema (DME), central serous chorioretinopathy (CSC), and wet age-related macular degeneration (wAMD)
Bold lines represent the mean spectra for each group, with shaded regions indicating standard deviation. Major Raman peaks are highlighted with alternating blue and red vertical bands and matching-colored numerical labels, corresponding to biomolecular assignments listed in Table 2. (b) Principal component analysis (PCA) score plot based on the first three components. Classification using PC1 to PC3 yielded an accuracy of 43.95%, indicating limited discriminative capability. (c) Variance distribution across principal components. Cumulative variance approached 88% by the 50th component and exceeded 91% by the 100th component.

Table 2
Raman peak assignments observed in aqueous humor samples from patients with RVO, DME, CSC, and wAMD.

Peak (cm^{-1})	Assignment	Reference
375	Valine	[23]
420	Tyrosine	[23,24]
501	Glycine	[23,25]
530	Glutamate	[23,26]
640	Tyrosine	[24,27]
685	Glycine	[23,25]
750	Valine	[23,28]
830	Tyrosine	[27,29]
855	Proline	[27,29]
930	Proline and valine	[23,27]
1000	Phenylalanine	[23,27]
1050	Glycogen	[27,30]
1135	Serine	[23]
1265, 1300	Fatty acids	[27,31]
1345	Valine	[23]
1405	Glutamate	[23,26]
1550	Proline	[23,27]
1600	Phenylalanine	[23,27]
1655	Fatty acids/Amide I (proteins)	[27,31]
2095, 2120	CN stretching-related vibration	[27,32]

RVO: retinal vein occlusion; DME: diabetic macular edema; CSC: central serous chorioretinopathy; wAMD: wet age-related macular.

PC1–PC3 collectively accounted for 65.84% of the total variance, their diagnostic separability remained limited, yielding a classification accuracy of only 43.95%.

For example, the cumulative variance plot in Fig. 2c showed that approximately 91% of the variability is not captured until around the 100th principal component. This suggests that informative spectral differences are dispersed across higher-order components, rather than being concentrated in the most dominant axes. Such a distribution implies that meaningful diagnostic cues may reside within subtle, high-dimensional features and underscores the need for supervised or AI-based modeling to detect fine-grained biochemical patterns that linear unsupervised projections cannot resolve.

3.5. Multi-stage AI framework for RVD screening and differential diagnosis using PC-SVM, LDA, and QDA

Supervised classification was performed to differentiate Raman spectra from five clinical groups using principal component–based linear discriminant analysis (PC-LDA) and quadratic discriminant analysis (PC-QDA). The PC-LDA model produced discernible separation boundaries when 50 PCs were used, reflecting partially distinct biochemical signatures among disease groups, as shown in Fig. 3a. The resulting classification yielded a discriminant accuracy of 92.35%, as summarized in the confusion matrix in Fig. 3b. We implemented a 10-fold cross-validation (CV) approach to rigorously evaluate the model's resistance to overfitting and ensure its generalizability. In this framework, the dataset was randomly partitioned into ten subsets, where nine subsets (90%) were used for training, and the remaining subset (10%) served as an independent validation set. The process was repeated ten times. This analysis revealed a maximal 10-fold CV score of 87.63% at 50 PCs, followed by divergence between discriminant accuracy and CV results with additional PCs (Fig. 3c). This widening gap signifies reduced generalizability, indicating that linear boundaries become insufficient for complex, high-dimensional spectral patterns as excessive PCs increase sensitivity to noise, resulting in overfitting.

To mitigate this risk, the number of PCs in each classifier was determined based on the convergence and stabilization of 10-fold CV accuracy. The point at which CV performance becomes progressively flatter represents a transition from informative variability to noise-driven variance. The selection of PCs at this plateau's onset is advantageous for preventing overfitting and reducing computational burden, as excessively large PC sets increase feature dimensionality without adding meaningful biochemical information. Even as patient recruitment expands, unnecessary decomposition of high-dimensional Raman spectra introduces redundant variables that increase model complexity without diagnostic benefit. This redundancy slows computation and inflates classifier complexity.

In contrast to LDA, the nonlinear PC-QDA model exhibited superior scalability with high dimensionality of spectral biomarkers. As illustrated in Fig. 3d and e, QDA generated curved decision boundaries that more accurately reflected biochemical overlap among disease conditions, achieving a discriminant accuracy of 98.24% and a peak 10-fold CV score of 86.45% at 30 PCs (Fig. 3f). This convergence remained stable beyond approximately 30 PCs, indicating enhanced resistance to

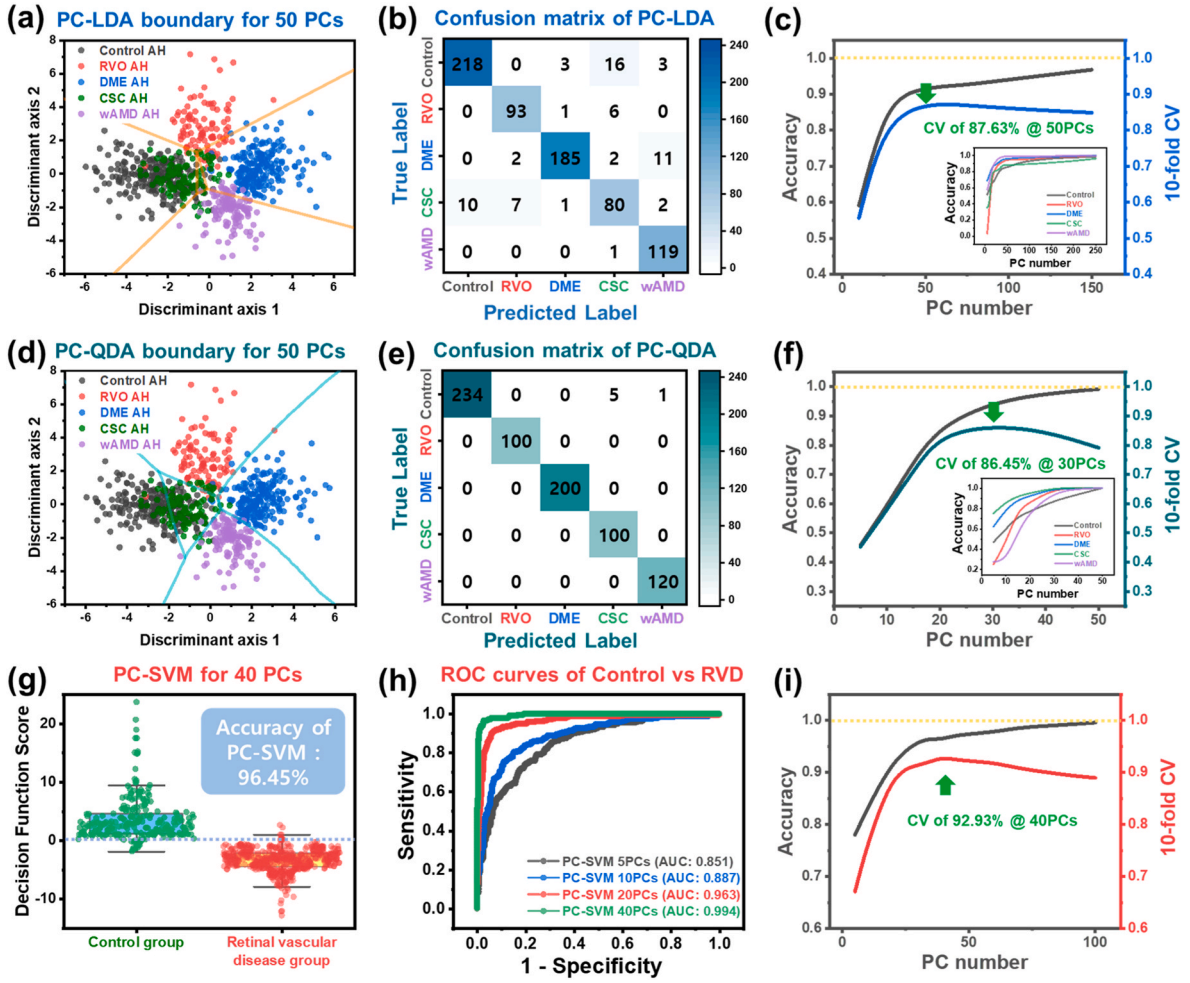

Fig. 3. Performance comparison of PC-LDA, PC-QDA, and PC-SVM models for classifying aqueous humor (AH) Raman spectra
(a) Decision boundaries of the PC-LDA model constructed using 50 principal components (PCs). (b) Confusion matrix of PC-LDA classification across the five clinical groups. (c) Accuracy and 10-fold cross-validation (CV) trends of PC-LDA as a function of PC number, achieving a CV accuracy of 87.63% at 50 PCs. (d) PC-QDA classification boundaries for 50 PCs, illustrating nonlinear decision surfaces. (e) Confusion matrix of PC-QDA classification showing enhanced intergroup discrimination. (f) Accuracy and 10-fold CV progression of PC-QDA, reaching a peak CV accuracy of 86.45% at 30 PCs. (g) PC-SVM decision function scores for binary classification between the control and retinal vascular disease (RVD) groups, achieving 96.45% accuracy with 40 PCs. (h) ROC curves of the PC-SVM model as a function of PC numbers, showing an optimal AUC of 0.994 at 40 PCs. (i) Accuracy and 10-fold CV trends for PC-SVM, highlighting a maximal CV accuracy of 92.93% using 40 PCs.

overfitting owing to QDA's ability to estimate distinct covariance structures for each diagnostic class. Such flexibility enables better modeling of subtle shifts in Raman signals arising from lipids, proteins, and nucleic acid components that are shared but differentially expressed across retinal vascular diseases.

We performed n-fold cross-validation using the PC-LDA model at 50 PCs to further demonstrate that the model's performance is consistent and independent of specific training/test splits. The results showed remarkably stable accuracy regardless of the training data ratio: 87.63% for 10-fold (90% training), 87.89% for 5-fold (80% training), 87.37% for 4-fold (75% training), and 86.84% for 2-fold (50% training). The minimal variance in accuracy of $<1.1\%$ across different folds, even when using only 50% of the data for training, statistically confirms that the current dataset is sufficient to achieve a stable and generalized discriminant boundary. This stability significantly mitigates the risk of overfitting and substantiates the clinical reliability of the AI-assisted SERS platform for retinal disease diagnosis.

We further optimized our diagnostic framework by incorporating an SVM algorithm focused on the primary identification of RVD to establish a highly efficient clinical screening protocol. While detailed multiclass differentiation is valuable for subtyping, the initial clinical priority is often the high-sensitivity screening of candidates with RVD who require immediate medical intervention, such as anti-VEGF therapy. To this end, we performed a binary classification between the healthy control group and RVD group to maximize the diagnostic utility of our SERS platform (Fig. 3g–i).

The PC-SVM model achieved an outstanding diagnostic accuracy of 96.45% with 40 PCs, as illustrated in Fig. 3g. Unlike multiclass models, this binary approach specifically enables the derivation of critical screening metrics, including sensitivity and specificity, which are paramount for first line clinical diagnostics. ROC analysis (Fig. 3h) confirmed the robustness of this screening strategy, with the AUC reaching 0.994 at 40 PCs. These results demonstrate that the SVM-integrated SERS platform is optimally designed to function as a biochemical gatekeeper, identifying patients in need of treatment with exceptional precision even before structural changes are detectable by conventional imaging. Consequently, this strategic inclusion of binary SVM analysis provides a more actionable clinical workflow, bridging the gap between initial screening and personalized therapeutic interventions.

Furthermore, the robustness of this screening approach was statistically validated through 10-fold CV, as shown in Fig. 3i. While the

multiclass LDA and QDA models achieved cross-validated accuracies of 87.63% and 86.45% respectively, the PC-SVM model demonstrated superior generalization performance, reaching a peak CV accuracy of 92.93% at 40 PCs (Fig. 3i). This significant improvement in CV accuracy indicates that the SVM algorithm effectively captures the most discriminative biochemical features of RVD while maintaining high resistance to overfitting.

3.6. *Spectral stratification of treatment response in retinal vascular diseases*

We investigated the treatment response stratification using pre- and post-anti-VEGF aqueous humor samples to evaluate whether label-free SERS spectra can reflect therapeutic outcomes in RVD. Patients with RVO, DME, CSC, and wAMD were categorized into responder and non-responder groups based on standard clinical response criteria. For each

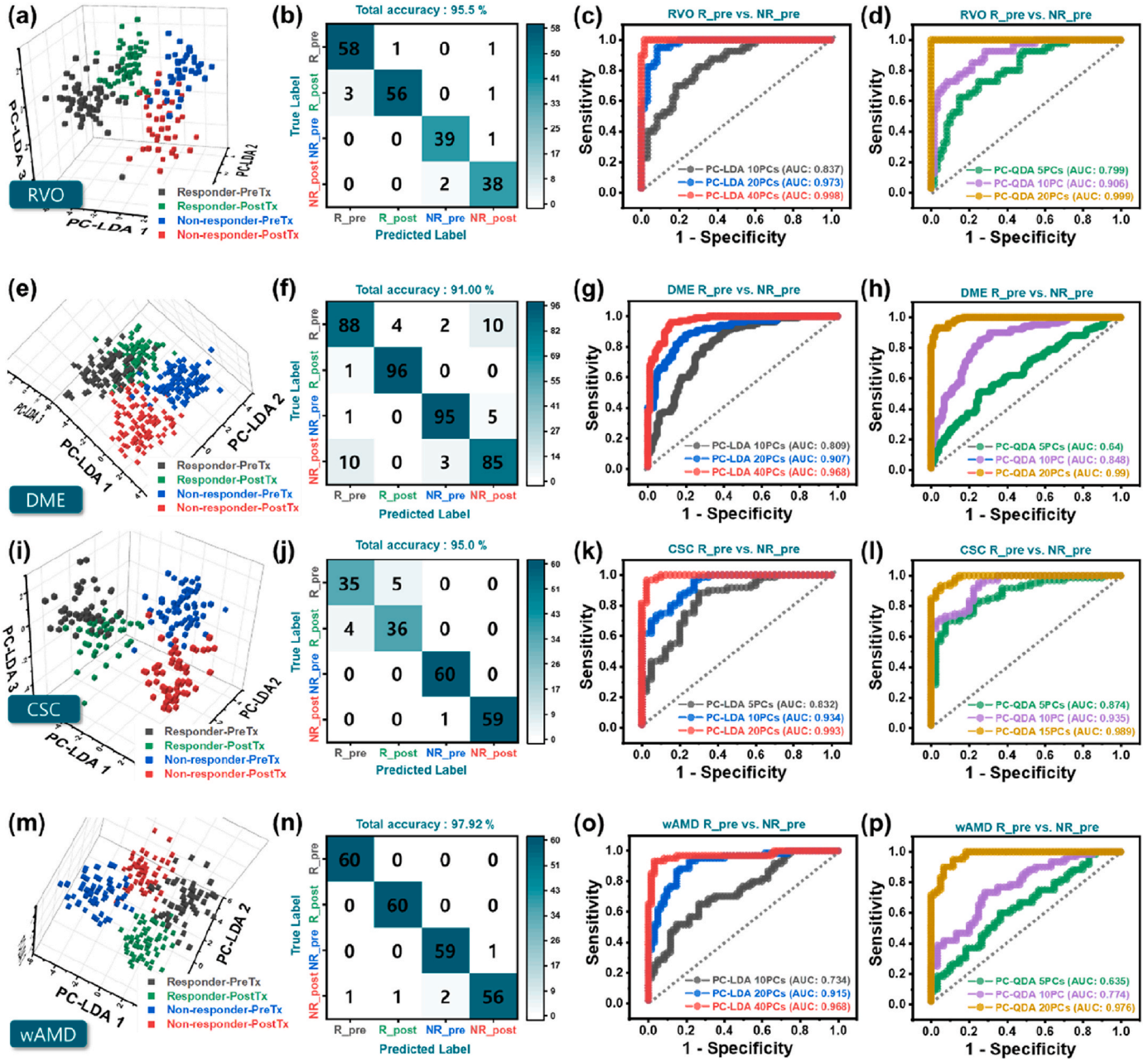

Fig. 4. Classification of treatment response in retinal vascular diseases using SERS-based principal component–linear discriminant analysis (PC-LDA) and quadratic discriminant analysis (PC-QDA) modeling
(a, b) PC-LDA 3D score plot and confusion matrix for retinal vein occlusion (RVO), based on spectral data from responder and non-responder groups before and after anti-VEGF treatment. Receiver operating characteristic (ROC) curves evaluating RVO responder vs. non-responder classification performance using (c) PC-LDA and (d) PC-QDA. Increasing the number of principal components (10, 20, 40 for LDA; 10, 30, 50 for QDA) enhances the area under the curve (AUC). (e, f) PC-LDA 3D score plot and confusion matrix for diabetic macular edema (DME) samples. ROC curves for DME, comparing responder vs. non-responder groups using (g) PC-LDA and (h) PC-QDA across increasing PC dimensions. (i, j) PC-LDA score plot and corresponding confusion matrix for central serous chorioretinopathy (CSC). ROC curves illustrating classification between CSC responders and non-responders using (k) PC-LDA and (l) PC-QDA models. (m, n) PC-LDA 3D score plot and confusion matrix for wet age-related macular degeneration (wAMD) samples, categorized into the four treatment response groups.
(o, p) ROC curves for wAMD responder vs. non-responder comparison. (o) shows PC-LDA models using 10, 20, and 40 principal components; (p) shows PC-QDA results using 10, 30, and 50 components.

condition, supervised machine learning models were trained on PCA-reduced spectral data, and classification was performed using PC-LDA and PC-QDA. The results are summarized in Fig. 4a–p.

Regarding RVO (Fig. 4a–d), the PC-LDA model using the top 100 PCs yielded distinguishable clustering between responders and non-responders, as shown in the 3D score plot. The confusion matrix confirmed that classification was largely accurate, with misclassification occurring primarily in borderline cases. ROC analysis showed that the AUC increased with the number of PCs, reaching above 0.95 at 40 PCs for LDA. The PC-QDA model further improved performance, achieving AUC values nearing 0.99 at 50 PCs (Fig. 4d), indicating that nonlinear classification boundaries better capture the spectral nuances associated with treatment response.

A similar pattern was observed for DME (Fig. 4e–h). Clear spectral differentiation between responder and non-responder groups emerged in both LDA and QDA score spaces; however, the distinction was somewhat more diffuse compared to RVO. The confusion matrix for QDA demonstrated balanced sensitivity and specificity, and ROC curves showed consistent AUC improvement with increased PC dimensionality. Spectral changes after treatment were more pronounced in responders for both LDA and QDA, suggesting that treatment-induced molecular alterations are more readily detected in successfully treated eyes.

The classification was more challenging for CSC (Fig. 4i–l). Score plots showed partial overlap between groups, particularly in LDA models, reflecting subtler molecular changes post-treatment. However, QDA provided better separation, and the AUC curves indicated stable performance beyond 30 PCs. Classification metrics were modestly lower compared to RVO and DME; nonetheless, the results support the feasibility of using SERS to detect therapeutic response signatures in patients with CSC.

Regarding wAMD (Fig. 4m–p), patients were stratified into four treatment response categories based on established clinical guidelines. Despite the increased complexity of multi-class prediction, the PC-LDA model provided recognizable clustering, and the confusion matrix revealed that most misclassifications occurred between adjacent response levels. QDA significantly enhanced classification accuracy, effectively resolving the multi-group structure. ROC analysis indicated robust class separability, with the highest AUC values observed at 50 PCs.

Overall, our findings demonstrated that SERS-based spectral profiles of aqueous humor can capture subtle but clinically relevant biochemical signatures associated with anti-VEGF treatment response. The superior performance of QDA highlights the inherent nonlinearity in these molecular changes and reinforces the advantage of high-dimensional, AI-enabled spectral analysis for personalized therapy stratification in retinal diseases.

3.7. Clinical relevance of SERS signal profiling and its implementation in medical settings

The clinical significance of our SERS-based signal analysis is its ability to translate complex molecular shifts into a definitive diagnostic fingerprint for RVD. Specifically, spectral variations at 501 and 640 cm^{-1} are closely associated with the disulfide bridging (S-S) and C-S stretching modes of dominant serum proteins such as albumin, which act as primary markers for vascular leakage into the AH [27,33]. Furthermore, the intensity shifts in the 1345–1405 cm^{-1} range correspond to the aliphatic side chains of apolipoproteins, reflecting the altered lipid metabolism and increased vascular permeability observed in patients with DME and wAMD [34,35]. These spectral signatures, collectively captured as high-dimensional patterns at 1655 cm^{-1} (Amide I), demonstrate that our AI-integrated platform provides a "reasonable diagnostic bridge" by probing the pathophysiological restructuring of the intraocular proteome without necessitating the isolation of individual biomarkers.

This interpretative framework is further supported by the data distribution observed in Fig. 3a and d, where CSC samples are positioned in close proximity to the control group compared to the distinct clusters of DME or wAMD. This spatial overlap suggests that the intraocular molecular environment in CSC remains relatively preserved because the influx of large serum macromolecules is attenuated. Such a phenomenon is consistent with the localized retinal pigment epithelium (RPE) dysfunction of CSC rather than the extensive blood-retinal barrier breakdown found in other RVDs. These results underscore that the degree of serum-derived marker infiltration is a primary determinant of our platform's ability to categorize high-dimensional biochemical patterns into specific disease phenotypes.

Beyond its diagnostic accuracy, this platform offers substantial value for early screening and formulating personalized therapeutic strategies. In routine ophthalmological practice, patients presenting with non-specific symptoms such as blurred vision may have combined corneal or media opacities, which may limit imaging diagnosis. Therefore, this platform may provide an early and accurate diagnosis of retinal conditions especially in cases when imaging is limited. Furthermore, the platform's capacity to identify specific biochemical shifts associated with anti-VEGF resistance enables the differentiation of responders and non-responders at an early stage. By moving beyond a "trial-and-error" approach, this technology enables clinicians to more effectively select optimal therapeutic agents, thereby facilitating timely intervention and improving long-term visual outcomes for patients who might otherwise face irreversible vision loss.

The practical implementation of this technology is driven by the synergy between nanostructure-based sensing chips and AI-driven software, offering distinct advantages over conventional multi-omics. Traditional proteomics and metabolomics often require large sample volumes and complex pretreatment methods, rendering them nearly impossible to apply to the trace amounts of biospecimens typically obtained from AH. In contrast, our nanostructure-based sensor enables ultrasensitive detection from minimal volumes of < 5 μL. The nanostructures act as both a selective filter for biomolecules and a source of dramatic signal enhancement, capturing high-fidelity information that remains inaccessible to standard omics techniques. By automating data processing, this system functions as a robust and cost-effective point-of-care diagnostic tool for real-world clinical environments.

Despite these clinical advantages, certain limitations should be noted. First, as this study was conducted on a relatively small cohort at a single clinical center, larger multi-center trials are required to further validate the generalizability of our SERS-AI framework. Additionally, potential confounding effects from systemic medications or long-term metabolic backgrounds should be further explored in future studies to enhance the platform's robustness for real-world clinical translation.

4. Conclusion

This study demonstrated that an AI-assisted SERS platform using gold-coated ZnO nanorod substrates provides a clinically validated strategy for biochemical diagnosis and treatment monitoring in RVDs. The platform sensitively captured disease-associated biochemical heterogeneity without labeling or enzymatic preparation by extracting reproducible vibrational signatures from microliter-scale aqueous humor samples (<5 μL). These signals were acquired under an IRB-approved prospective protocol using clinically defined imaging criteria, ensuring that biochemical classifications were based on robust ophthalmic diagnostics rather than solely on spectral variation.

Integration with machine learning translated high-dimensional biochemical spectra into clinically meaningful classifications. The PC-SVM model achieved an outstanding primary screening accuracy of 96.45% for RVD identification, with a 10-fold CV accuracy of 92.93% and an AUC of 0.994. For multiclass differentiation, nonlinear PC-QDA modeling closely aligned with multimodal imaging diagnoses, producing a stable 10-fold CV score of 86.45% at 30 PCs and demonstrating high resistance to overfitting. Additionally, Raman-derived biochemical

profiles predicted anti-VEGF therapeutic response with over 90% accuracy before OCT-visible changes, a finding supported by longitudinal comparisons of CST and BCVA trajectories. This demonstrates that biochemical alterations precede structural recovery and that the platform can guide earlier therapeutic decisions using real patient outcomes as ground truth.

Taken together, these findings establish AH-based SERS combined with supervised AI interpretation as a validated clinical method capable of classifying RVDs and identifying treatment response from trace ocular fluid. This confirms that microliter-scale aqueous humor can serve as a practical source of clinically meaningful biochemical information when supported by standardized acquisition and quantitative spectral modeling.

To the best of our knowledge, no studies have distinguished retinal and choroidal vascular diseases and their treatment responses through biochemical profiling of aqueous humor using Raman spectroscopy. Current diagnostic paradigms heavily rely on structural imaging, which cannot fully reflect the underlying biochemical dynamics influencing therapeutic response. We focused on this unmet need for a diagnostic and therapeutic approach that offers high biochemical specificity and sensitivity, with minimal invasiveness and real-time compatibility in clinical ophthalmology. This work introduces a novel method to detect pre-treatment molecular signatures associated with treatment efficacy by analyzing microliter-scale aqueous humor using Raman spectroscopy. Such biochemical insights facilitate the earlier and more accurate identification of responders and non-responders, enabling more cost-effective, personalized anti-VEGF therapy. Raman spectroscopy can enhance individualized treatment selection and improve clinical efficiency by offering a minimally invasive, rapid, and highly specific biochemical assessment. This framework may ultimately bridge the gap between structural biomarkers and true biochemical disease activity in retinal disease management.

Declaration of generative AI and AI-assisted technologies in the writing process

During the preparation of this work, the authors used Gemini in order to improve language and readability. After using this tool/service, the authors reviewed and edited the content as needed and take full responsibility for the content of the published article.

Funding

This work was supported by the Ministry of Science, ICT and Future Planning (MSIP) through the National Research Foundation of Korea (NRF) (RS-2024-00450201, RS-2025-25407039, RS-2026-25475564), also supported by a grant from the Korea Health Technology R&D Project through the Korea Health Industry Development Institute (KHIDI), funded by the Ministry of Health and Welfare, Republic of Korea (RS-2024-00438689 RS-2026-25516119).

CRediT authorship contribution statement

Sanghwa Lee: Data curation, Formal analysis, Investigation, Methodology, Validation, Visualization, Writing – original draft. **Yong-Ha Jo:** Data curation, Investigation, Resources, Validation, Visualization, Writing – original draft. **Kyeong Ryeol Kim:** Data curation, Investigation, Resources, Software. **Junyeop Lee:** Conceptualization, Funding acquisition, Methodology, Supervision, Validation, Writing – original draft. **Jun Ki Kim:** Conceptualization, Formal analysis, Funding acquisition, Investigation, Supervision, Validation, Writing – original draft, Writing – review & editing.

Declaration of competing interest

J.K.K. is a scientific advisor to the startup Apollon Inc. (Korea), which may develop diagnostic devices based on this work. The authors declare no other competing interests.

Appendix A. Supplementary data

Supplementary data to this article can be found online at https://doi.org/10.1016/j.mtadv.2026.100810.

Data availability

Data will be made available on request.

References

[1] P.A. Campochiaro, Retinal and choroidal vascular diseases: past, present, and future: the 2021 proctor lecture, Investig. Ophthalmol. Vis. Sci. 62 (2021) 26, https://doi.org/10.1167/iovs.62.14.26.
[2] H. Hashemi, R. Pakzad, A. Yekta, M. Aghamirsalim, M. Pakbin, S. Ramin, M. Khabazkhoob, Global and regional prevalence of age-related cataract: a comprehensive systematic review and meta-analysis, Eye (Lond.) 34 (2020) 1357–1370, https://doi.org/10.1038/s41433-020-0806-3.
[3] C.R. Garcia-Cabrera, N.A. Afshari, Cataract surgery in patients with diabetes mellitus: preoperative, intraoperative, and postoperative considerations, Curr. Opin. Ophthalmol. 37 (2026) 42–47, https://doi.org/10.1097/ICU.0000000000001184.
[4] C.J. Chu, R.L. Johnston, C. Buscombe, A.B. Sallam, Q. Mohamed, Y.C. Yang, G. United, Kingdom pseudophakic macular edema study, risk factors and incidence of macular edema after cataract surgery: a database study of 81984 eyes, Ophthalmology 123 (2016) 316–323, https://doi.org/10.1016/j.ophtha.2015.10.001.
[5] U. Schmidt-Erfurth, A. Sadeghipour, B.S. Gerendas, S.M. Waldstein, H. Bogunovic, Artificial intelligence in retina, Prog. Retin. Eye Res. 67 (2018) 1–29, https://doi.org/10.1016/j.preteyeres.2018.07.004.
[6] S.M. Hariprasad, F.G. Holz, C.V. Asche, A. Issa, O. Mora, S. Keady, M.F. Rezk, P. Sarocco, S. Simoens, Clinical and socioeconomic burden of retinal diseases: can biosimilars add value? A narrative review, Ophthalmol Ther 14 (2025) 621–641, https://doi.org/10.1007/s40123-025-01104-3.
[7] J.O. Wallsh, R.P. Gallemore, Anti-VEGF-Resistant retinal diseases: a review of the latest treatment options, Cells 10 (2021), https://doi.org/10.3390/cells10051049.
[8] P.J. Rodriguez-Valdes, M. Rehak, D. Zur, A. Sala-Puigdollers, S. Fraser-Bell, M. Lupidi, J. Chhablani, Z. Cebeci, I. Lains, V. Chaikitmongkol, A.T. Fung, M. Okada, J.D. Unterlauft, L. Smadar, A. Loewenstein, M. Iglicki, C. Busch, GRAding of functional and anatomical response to DExamethasone implant in patients with diabetic macular edema: GRADE-DME study, Sci. Rep. 11 (2021) 4738, https://doi.org/10.1038/s41598-020-79288-w.
[9] A. Gigon, A. Iskandar, S. Kasser, S. Naso, M. Zola, I. Mantel, Short-term response to anti-VEGF as indicator of visual prognosis in refractory age-related macular degeneration, Eye (Lond.) 38 (2024) 1342–1348, https://doi.org/10.1038/s41433-023-02900-6.
[10] R.S. Kailar, B.L. Kuo, S.W. Perkins, R.P. Singh, Long-term outcomes in early versus limited response to Anti-VEGF treatment for retinal vein occlusion, Ophthalmol Retina 8 (2024) 55–61, https://doi.org/10.1016/j.oret.2023.08.005.
[11] S. Lee, M. Jue, M. Cho, K.H. Lee, B. Paulson, H. Jo, J.S. Song, S.J. Kang, J.K. Kim, Label-free atherosclerosis diagnosis through a blood drop of apolipoprotein E knockout mouse model using surface-enhanced Raman spectroscopy validated by machine learning algorithm, Bioeng. Transl. Med. 8 (2023), https://doi.org/10.1002/btm2.10529.
[12] S. Lee, H. Kwon, J. Oh, K.R. Kim, J. Hwang, S. Kang, K. Lee, J.M. Namgoong, J. K. Kim, Post-Transplant liver monitoring utilizing integrated surface-enhanced raman and AI in hepatic ischemia-reperfusion injury animal model, Int J Nanomedicine 20 (2025) 6743–6755, https://doi.org/10.2147/IJN.S497900.
[13] S. Lee, J. Oh, K. Lee, M. Cho, B. Paulson, J.K. Kim, Diagnosis of ischemic renal failure using surface-enhanced raman spectroscopy and a machine learning algorithm, Anal. Chem. 94 (2022) 17477–17484, https://doi.org/10.1021/acs.analchem.2c03634.
[14] S. Lee, M. Jue, K. Lee, B. Paulson, J. Oh, M. Cho, J.K. Kim, Early-stage diagnosis of bladder cancer using surface-enhanced Raman spectroscopy combined with machine learning algorithms in a rat model, Biosens. Bioelectron. 246 (2024), https://doi.org/10.1016/j.bios.2023.115915.
[15] S.H. Lee, J.M. Kim, K.H. Lee, H.Y. Cho, S. Shin, J.K. Kim, Diagnosis and classification of kidney transplant rejection using machine learning-assisted surface-enhanced Raman spectroscopy using a single drop of serum, Biosens. Bioelectron. 261 (2024), https://doi.org/10.1016/j.bios.2024.116523.
[16] M. Tamhane, S. Cabrera-Ghayouri, G. Abelian, V. Viswanath, Review of biomarkers in ocular matrices: challenges and opportunities, Pharm. Res. 36 (2019) 40, https://doi.org/10.1007/s11095-019-2569-8.
[17] B. Titz, J. Siebourg-Polster, F. Bartolo, V. Lavergne, Z. Jiang, J. Gayan, L. Altay, P. Enders, C. Schmelzeisen, Q.T. Ippisch, M.J. Koss, S. Ansari-Shahrezaei, J. G. Garweg, S. Fauser, A. Dieckmann, Implications of ocular confounding factors for aqueous humor proteomic and metabolomic analyses in retinal diseases, Transl. Vis. Sci. Technol. 13 (2024) 17, https://doi.org/10.1167/tvst.13.6.17.

[18] W.C. Chang, C.H. Lee, S.H. Chiou, C.C. Liao, C.W. Cheng, Proteomic analysis of aqueous humor proteins in Association with cataract risks: diabetes and smoking, J. Clin. Med. 10 (2021), https://doi.org/10.3390/jcm10245731.
[19] L. Wu, J. An, X. Li, Q. Tao, Z. Liu, K. Zhang, L. Zhou, X. Zhang, Comprehensive proteomic profiling of aqueous humor in idiopathic uveitis and vogt-koyanagi-harada syndrome, ACS Omega 9 (2024) 18643–18653, https://doi.org/10.1021/acsomega.3c10257.
[20] W.J. Qian, J.M. Jacobs, T. Liu, D.G. Camp 2nd, R.D. Smith, Advances and challenges in liquid chromatography-mass spectrometry-based proteomics profiling for clinical applications, Mol. Cell. Proteomics 5 (2006) 1727–1744, https://doi.org/10.1074/mcp.M600162-MCP200.
[21] K. Kitsu, K. Shinoda, Y. Mizuno, K. Yagura, G. Terauchi, C.S. Matsumoto, M. Ochi, A. Mizota, Effect of paracentesis on retinal function associated with changes in intraocular pressure caused by intravitreal injections, Transl. Vis. Sci. Technol. 9 (2020) 10, https://doi.org/10.1167/tvst.9.9.10.
[22] S. Lee, S.H. Lee, B. Paulson, J.C. Lee, J.K. Kim, Enhancement of local surface plasmon resonance (LSPR) effect by biocompatible metal clustering based on ZnO nanorods in Raman measurements, Spectoc. Acta Pt. A-Molec. Biomolec. Spectr. 204 (2018) 203–208, https://doi.org/10.1016/j.saa.2018.06.045.
[23] J. De Gelder, K. De Gussem, P. Vandenabeele, L. Moens, Reference database of Raman spectra of biological molecules, J. Raman Spectrosc. 38 (2007) 1133–1147, https://doi.org/10.1002/jrs.1734.
[24] B. Hernández, Y. Coïc, F. Pflüger, S. Kruglik, M. Ghomi, All characteristic Raman markers of tyrosine and tyrosinate originate from phenol ring fundamental vibrations, J. Raman Spectrosc. 47 (2016) 210–220, https://doi.org/10.1002/jrs.4776.
[25] J. Baran, H. Ratajczak, Polarised IR and Raman spectra of the gamma-glycine single crystal, Spectrochim. Acta Mol. Biomol. Spectrosc. 61 (2005) 1611–1626, https://doi.org/10.1016/j.saa.2004.11.064.
[26] N. Peica, C. Lehene, N. Leopold, S. Schlücker, W. Kiefer, Monosodium glutamate in its anhydrous and monohydrate form:: differentiation by Raman spectroscopies and density functional calculations, Spectoc. Acta Pt. A-Molec. Biomolec. Spectr. 66 (2007) 604–615, https://doi.org/10.1016/j.saa.2006.03.037.
[27] A.C.S. Talari, Z. Movasaghi, S. Rehman, I.U. Rehman, Raman spectroscopy of biological tissues, Appl. Spectrosc. Rev. 50 (2015) 46–111, https://doi.org/10.1080/05704928.2014.923902.
[28] S. Pandiarajan, M. Umadevi, R. Rajaram, V. Ramakrishnan, Infrared and Raman spectroscopic studies of L-valine L-valinium perchlorate monohydrate, Spectoc. Acta Pt. A-Molec. Biomolec. Spectr. 62 (2005) 630–636, https://doi.org/10.1016/j.saa.2005.02.008.
[29] N. Stone, C. Kendall, N. Shepherd, P. Crow, H. Barr, Near-infrared Raman spectroscopy for the classification of epithelial pre-cancers and cancers, J. Raman Spectrosc. 33 (2002) 564–573, https://doi.org/10.1002/jrs.882.
[30] G. Shetty, C. Kendall, N. Shepherd, N. Stone, H. Barr, Raman spectroscopy: elucidation of biochemical changes in carcinogenesis of oesophagus, Br. J. Cancer 94 (2006) 1460–1464, https://doi.org/10.1038/sj.bjc.6603102.
[31] K. Czamara, K. Majzner, M.Z. Pacia, K. Kochan, A. Kaczor, M. Baranska, Raman spectroscopy of lipids: a review, J. Raman Spectrosc. 46 (2015) 4–20, https://doi.org/10.1002/jrs.4607.
[32] L.J.G.W. van Wilderen, D. Kern-Michler, H.M. Muller-Werkmeister, J. Bredenbeck, Vibrational dynamics and solvatochromism of the label SCN in various solvents and hemoglobin by time dependent IR and 2D-IR spectroscopy (vol 16, pg 19643, 2014), Phys. Chem. Chem. Phys. 19 (2017) 9676–9678, https://doi.org/10.1039/c7cp90063e.
[33] A. Rygula, K. Majzner, K.M. Marzec, A. Kaczor, M. Pilarczyk, M. Baranska, Raman spectroscopy of proteins: a review, J. Raman Spectrosc. 44 (2013) 1061–1076, https://doi.org/10.1002/jrs.4335.
[34] K. Huang, C. Schofield, T. Nguy, R. Dere, V. Wolowski, J. Siebourg-Polster, A. Dieckmann, J.G. Garweg, M. Chang, L. Honigberg, J. Hackney, V.B. Indjeian, Proteomics approach identifies aqueous humor biomarkers in retinal diseases, Commun. Med. 5 (2025) 134, https://doi.org/10.1038/s43856-025-00862-2.
[35] Y. Zhang, M. Xu, H. He, S. Ren, X. Chen, Y. Zhang, J. An, X. Ren, X. Zhang, M. Zhang, Z. Liu, X. Li, Proteomic analysis of aqueous humor reveals novel regulators of diabetic macular edema, Exp. Eye Res. 239 (2024) 109724, https://doi.org/10.1016/j.exer.2023.109724.